ACS APPLIED MATERIALS & INTERFACES

Research Article

Cite This: ACS Appl. Mater. Interfaces 2019, 11, 10462−10471

www.acsami.org

Probing the Aggregation and Immune Response of Human Islet Amyloid Polypeptides with Ligand-Stabilized Gold Nanoparticles

Ibrahim Javed,[†,§] Jiacheng He,[‡,§] Aleksandr Kakinen,[†] Ava Faridi,[†] Wen Yang,[‡] Thomas P. Davis,*[,†] Pu Chun Ke,*[,†] and Pengyu Chen*[,‡]

[†]ARC Centre of Excellence in Convergent Bio-Nano Science and Technology, Monash Institute of Pharmaceutical Sciences, Monash University, 381 Royal Parade, Parkville, VIC 3052, Australia

[‡]Materials Research and Education Center, Auburn University, Auburn, Alabama 36849, United States

Supporting Information

ABSTRACT: The use of nanomaterials has recently become an emerging strategy against protein amyloidosis associated with a range of metabolic and brain diseases. To facilitate research in this area, here we first demonstrated the use of hyperspectral imaging (HSI) and COMSOL simulations for reporting the aggregation of human islet amyloid polypeptides (IAPPs), a hallmark of type 2 diabetes, as well as the physical interactions between the peptide and gold nanoparticles (AuNPs) grafted with citrate and poly(ethylene glycol) (PEG_{400} and PEG_{3000}). We found a distinct anticorrelation between increased IAPP aggregation and decreased spectral red shifts incurred in the AuNP plasmonic resonance. Moreover, Jurkat cells exposed to IAPP and AuNPs were characterized by quantifying their cytokine secretions with a localized surface plasmon resonance (LSPR) immunoassay, where a peak response was registered for the most toxic IAPP oligomers and most suppressed by citrate-coated AuNPs. This study demonstrated the potential of using HSI and LSPR as two new platforms for the facile examination of protein aggregation and their induced immune response associated with amyloid diseases.

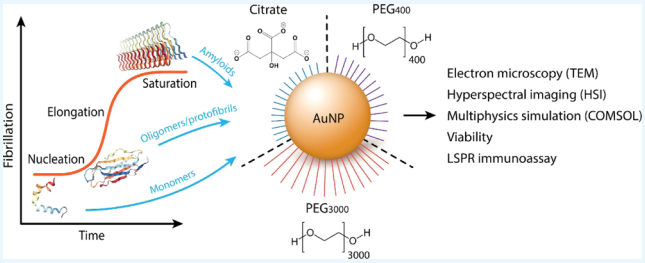

KEYWORDS: *IAPP, aggregation, gold nanoparticles, hyperspectral imaging, immunoassay*

INTRODUCTION

The human islet amyloid polypeptide (IAPP) is a 37-residue peptide co-synthesized and co-secreted with insulin by pancreatic β-cell islets.[1,2] In addition to its functional role in glycemic control, IAPP is closely associated with β-cell degeneration in type 2 diabetes (T2D), a metabolic disease and a global epidemic.[3] The aggregation of IAPP involves the transformation of functional IAPP monomers to oligomers, protofibrils, and amyloid fibrils. Although IAPP monomers are disordered in nature, IAPP oligomers, protofibrils, and fibrils are increasingly hydrophobic and rich in β sheets.[3] Biologically, IAPP in the oligomeric form is believed to be the most toxic,[4,5] whereas IAPP amyloids and plaques have been found in the islets of 90% T2D patients suggesting a causative process.[6] Overall, understanding the aggregation of IAPP, in a test tube or in the physiological environment, is of crucial importance for basic research on protein misfolding and for delineating the pathogenesis of T2D.

The kinetics of protein aggregation is often inferred from a thioflavin T (ThT) or a Congo red fluorescence assay, to report on the three stages of protein nucleation, elongation, and saturation on the pathway to the amyloid state. Direct observation of the aggregation states of amyloid proteins, in contrast, can be performed ex situ using atomic force microscopy, electron microscopy, and nuclear magnetic resonance or X-ray spectroscopies.[7−9] In addition, monoclonal antibodies, such as solanezumab, have been utilized for immunochemical detection of amyloid aggregation,[10] as in the Eli Lilly phase-3 clinical trial against Alzheimer's.[11,12] Antibodies such as aducanumab can bind to and clear amyloid plaques[13] but are selective against the conformation epitopes rather than the sequences of fibrils.[14−16] Overall, these methods, with the exception of the kinetic assays, require labor- and cost-intensive experimentation and data collection.

Recently, we have developed a biomimetic system of coating gold nanoparticles (AuNPs) with the amyloid fragments of whey protein β lactoglobulin (bLg).[17] The resulting functional bLg-AuNPs intercalated with IAPP through β-sheet stacking. This scheme, though effective in mitigating IAPP toxicity,[18] did not have the capacity of discerning the three major aggregation states, i.e., monomeric, oligomeric/protofibrillar, and fibrillar forms of amyloid proteins (Figure 1). Hyperspectral imaging (HSI) integrates high signal-to-noise dark-field microscopy with high-resolution scattering spectra for each pixel[19] and has been employed for food quality control and detection of the aggregation, cellular uptake, and

Received: November 6, 2018
Accepted: January 21, 2019
Published: January 21, 2019

DOI: 10.1021/acsami.8b19506
ACS Appl. Mater. Interfaces 2019, 11, 10462−10471

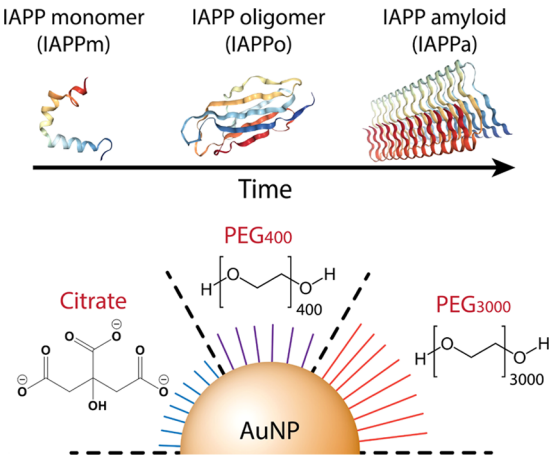

Figure 1. Design of the study, where monomeric, oligomeric/protofibrillar, and fibrillar IAPPs were brought into contact with AuNPs coated with citrate, PEG_{400}, and PEG_{3000}.

interaction of nanoparticles with proteins.[19−24] In this study, we first employed HSI to probe the three major aggregation states of IAPP via their interactions with ligand-stabilized gold nanoparticles (AuNPs) (Figure 1) and subsequently induced spectral shifts. Then, the responses of Jurkat human T cells to the three IAPP aggregation states as well as their associations with the AuNPs were examined, taking advantage of the high sensitivity of a localized surface plasmon resonance (LSPR) immunoassay for real-time, multiplex cytokine detection. These physical and biological characterizations facilitate the study of protein aggregation and therapeutic applications of nanomaterials against the toxicity of amyloid proteins.

RESULTS AND DISCUSSION

Syntheses of Ligand-Stabilized AuNPs. The AuNPs used in this study were stabilized by three types of hydrophilic ligands: citrate (Cit-, M.W. 189) and linear poly(ethylene glycol) (PEG) of 400 Da (PEG_{400}) and 3000 Da (PEG_{3000}) in molecular weight. The Cit, PEG_{400}, and PEG_{3000} AuNPs were measured by transmission electron microscopy (TEM) to be approximately 18−22 nm in size (Figures 2A and 3A). Citrate can stochastically adsorb and desorb from nanoparticles in suspension,[25] providing hydration to the AuNPs as well as competitive binding between the ligand and IAPP. PEG is a stealth polymer offering a steric separation of nanoparticles in aqueous solutions and preventing their recognition by opsonins of the immune system for prolonged blood circulation.[26−28] Here, PEG_{400} and PEG_{3000} rendered flexibility in modulating the aggregation of AuNPs as well as their interactions with IAPP. AuNPs, meanwhile, induced surface plasmon resonance (SPR) upon light excitation, which served as reporters of their immediate nanoenvironments, including that of adsorbed IAPP species.

Probing IAPP Aggregation States and Their Physical Interactions with AuNPs. The interactions of AuNPs with monomeric (abbreviated as IAPPm hereafter), oligomeric/protofibrillar (IAPPo), and fibrillar IAPP (IAPPa) imparted changes to the dielectric environment of the AuNPs and consequently induced SPR spectral shifts. The Cit, PEG_{400}, and PEG_{3000} AuNPs possessed increasing hydrodynamic sizes of 24.2−35.1 nm and ζ-potentials of −24.4 to −18.1 mV, indicating good suspensibility of all three types of nanoparticles (Table 1).

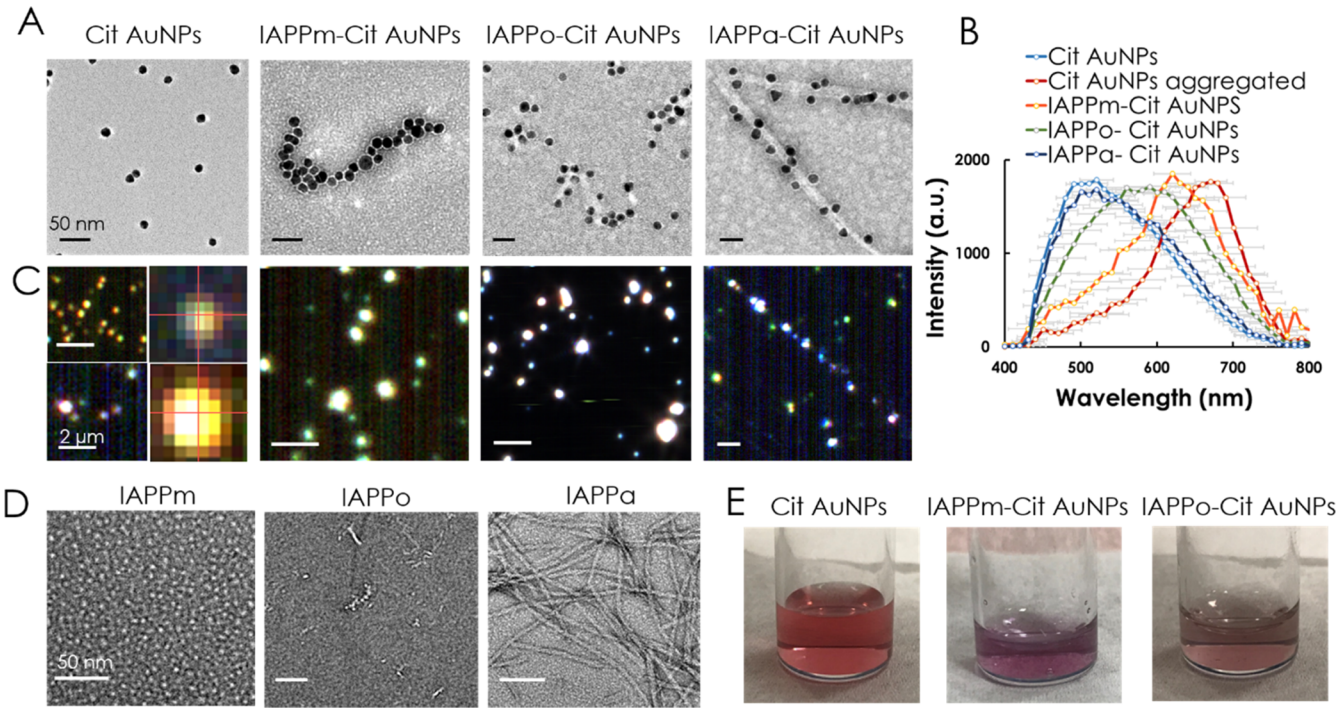

Figure 2. Interactions of Cit AuNPs with IAPP monomers (IAPPm), oligomers/protofibrils (IAPPo), and amyloid fibrils (IAPPa), observed with (A) TEM and (B, C) HSI. HSI analyses of pixels corresponding to single (up) and aggregated (down) Cit AuNPs are exemplified in the far-left panels of (C). (D) TEM of the three types of IAPP control species. Incubation of Cit AuNPs with IAPPm (middle) and IAPPo (right) induced color changes of the Cit AuNP suspension from wine red (left) to purple (middle) and light-purple (right) (E). Incubation: 5 min. Scale bars in (A) and (D): 50 nm. Scale bars in (C): 2 μm.

DOI: 10.1021/acsami.8b19506
ACS Appl. Mater. Interfaces 2019, 11, 10462−10471

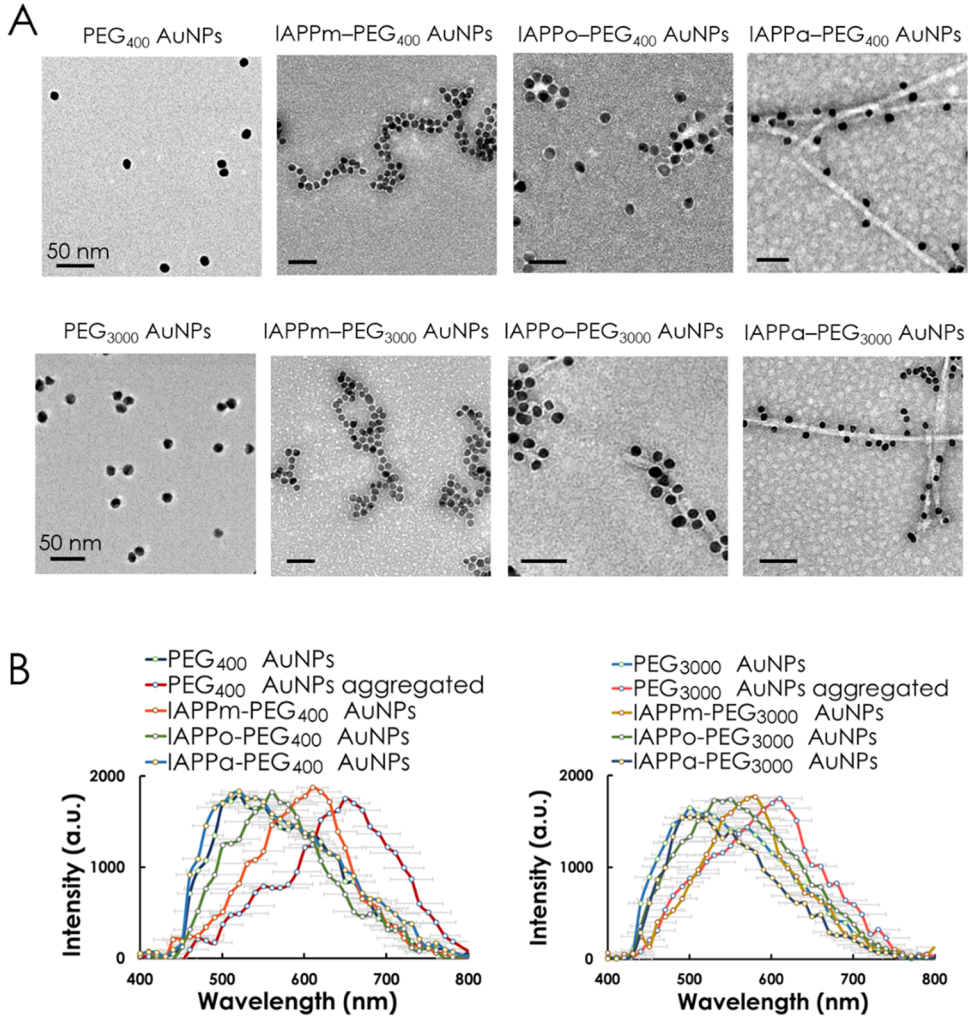

Figure 3. (A) Interaction of PEG_{400} and PEG_{3000} AuNPs with IAPP, observed with TEM. (B) Corresponding hyperspectral SPR shifts for PEG_{400} and PEG_{3000} AuNPs. IAPP: 25 μM. Incubation: 5 min.

Table 1. Hydrodynamic Sizes, Polydispersity Indexes (PDI), and ζ-Potentials of the Three Types of AuNPs[a]

parameters	Cit AuNPs	PEG_{400} AuNPs	PEG_{3000} AuNPs
size (nm)	24.2 ± 3.6	28.4 ± 1.9	35.1 ± 2.2
PDI	0.179	0.128	0.231
ζ-potential (mV)	−24.4 ± 3.4	−21.1 ± 3.8	−18.1 ± 4.6
$\Delta\lambda_m$ (nm)	122 ± 6	92 ± 7	76 ± 5
$\Delta\lambda_o$ (nm)	81 ± 5	53 ± 6	35 ± 4
$\Delta\lambda_a$ (nm)	22 ± 3	14 ± 4	9 ± 4

[a]The SPR spectral shifts of the AuNPs when incubated with IAPP monomers ($\Delta\lambda_m$), oligomers/protofibrils ($\Delta\lambda_o$), and amyloid fibrils ($\Delta\lambda_a$) are also tabulated.

The Cit, PEG_{400}, and PEG_{3000} AuNPs were monodispersed before interacting with IAPP, and immediately aggregated into small clusters upon 5 min of incubation with cationic IAPP monomers, driven by electrostatic and hydrophobic interactions (for Cit) as well as hydrogen bonding (for Cit, PEG_{400}, and PEG_{3000}) (Table S1). Clustering of the AuNPs by IAPP monomers into chainlike structures was revealed by TEM (Figures 2A and 3A), which was accompanied by concomitant color changes in the AuNP suspensions from wine red to purple/light-purple (Figure 2E).

IAPP oligomers/protofibrils and fibrils were prepared by incubating IAPP monomers at 4 °C for 5 h and at room temperature for 24 h, respectively. Incubating AuNPs with IAPP oligomers/thin protofibrils resulted in their association (Table S1; Figures 2A and 3A), although the AuNPs were less tightly packed than with IAPP monomers. No intercalation but surface adsorption was observed when incubating AuNPs with IAPP fibrils (Figure 2A). In addition, the toxicities of IAPPm and IAPPo in the presence and absence of the three types of AuNPs were examined and summarized in Figure S1, with a 14 h treatment of pancreatic βTC6 cells. As expected, IAPPm and IAPPo elicited significant toxicities to the cells, whereas their toxicities were alleviated by Cit, PEG_{400}, and PEG_{3000} AuNPs by ∼50−60% for the monomers and 40−50% for the oligomers, respectively. No significant toxicity was observed with IAPPa, whereas the presence of the AuNPs showed no effects on the toxicity of the fibrils (data not shown).

Accordingly, HSI revealed the SPR spectral shifts of the AuNPs, following the order of $\Delta\lambda_m > \Delta\lambda_o > \Delta\lambda_a$ for the nanoparticles incubated with IAPP monomers, oligomers/protofibrils, and fibrils, respectively (Figures 2B and 3B; Table 1). Furthermore, the most prominent SPR red shift upon binding with IAPP monomers was observed for Cit AuNPs, followed by that for PEG_{400} and PEG_{3000} AuNPs. The extents of the red shifts can be partially attributed to the different

DOI: 10.1021/acsami.8b19506
ACS Appl. Mater. Interfaces 2019, 11, 10462−10471

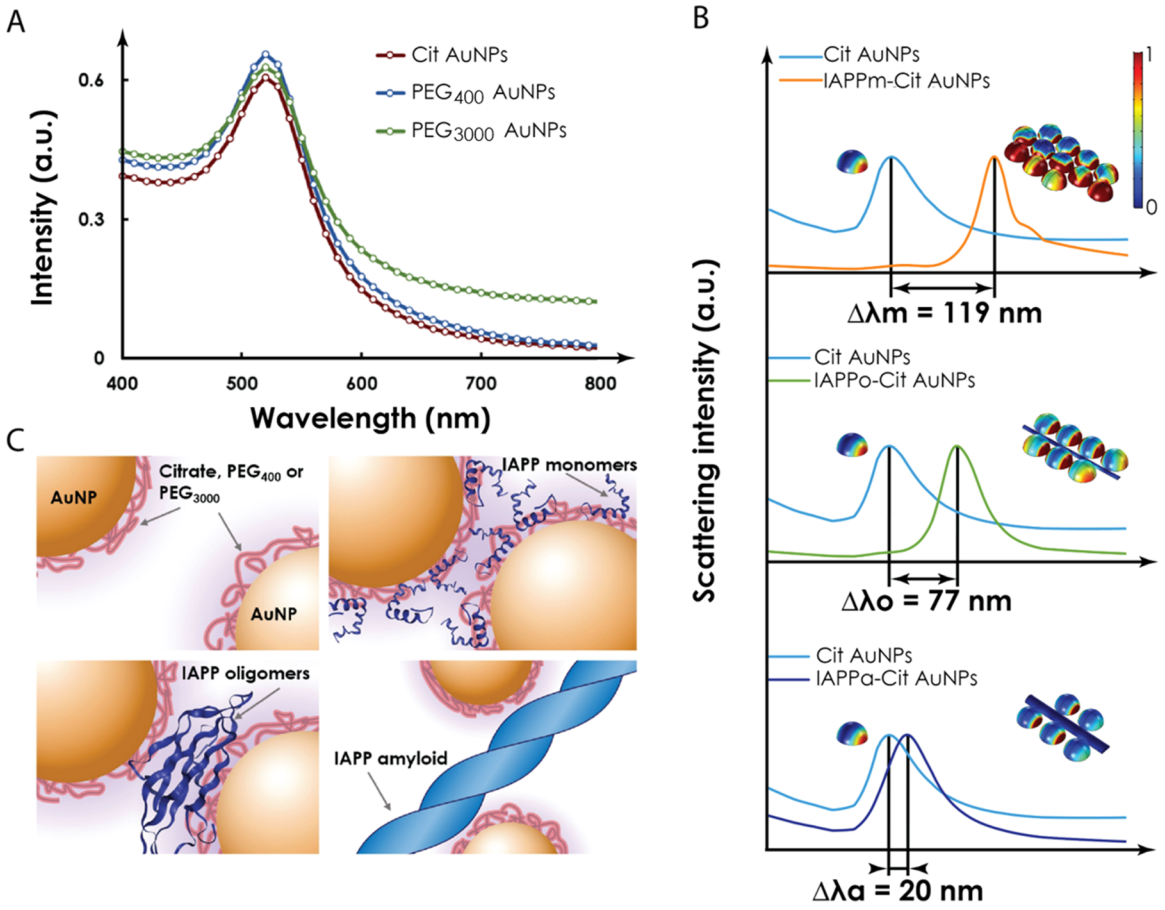

Figure 4. (A) Measured UV−vis absorbance of Cit, PEG_{400}, and PEG_{3000} AuNPs. (B) Simulated scattering spectra (normalized) and near-field scattering intensity distributions (insets) of Cit AuNPs, IAPPm−Cit AuNPs, IAPPo−Cit AuNPs, and IAPPa−Cit AuNPs. (C) Schematics of the spatial separations of AuNPs and their induced packing by the three types of IAPP species.

chain lengths/radii of gyration of the surface ligands, with Cit being the shortest and PEG_{3000} the longest. The stronger antifouling capacity of PEG_{3000} than PEG_{400} further discouraged tight packing of the AuNPs on the IAPP species. On the other hand, IAPP monomers were the most effective for promoting close packing of AuNPs. Consequently, steric separations among the AuNPs and their associations with the IAPP species translated to different efficiencies of plasmonic coupling upon light excitation.[29−31] On the basis of the above observations, an additional measurement was performed to determine the dependence of SPR spectral shifts on IAPP concentration using Cit AuNPs and IAPPm (0.01−25 μM). Specifically, IAPPm of 0.01 μM induced no spectral shift from the control of Cit AuNPs, and IAPPm of 0.1 μM caused a red shift of 50 nm, whereas IAPPm of 1−25 μM yielded comparable red shifts of ∼110 nm, likely due to the increasingly saturated surface coating of Cit AuNPs by IAPPm at 1 μM and above (Figure S2).

The UV−vis absorbance characteristics of Cit AuNPs, PEG_{400} AuNPs, and PEG_{4000} AuNPs are summarized and compared in Figure 4A. All three samples exhibited an identical extinction peak at ca. 520 nm, suggesting that the AuNPs were well dispersed in the suspensions. No spectral shifts were observed for the UV−vis absorbance of Cit AuNPs incubated with IAPPm of 0.01−1 μM, whereas red shifts of 5 and 40 nm were generated with IAPPm of 10 and 25 μM, respectively (Figure S3), significantly less sensitive than the single-particle-based HSI detection (Figure S2). Since HSI collects scattered light from samples, the scattering spectra of four models, i.e., a single AuNP, IAPPm−Cit AuNPs, IAPPo−Cit AuNPs, and IAPPa−Cit AuNPs, were simulated with COMSOL. A 20 nm red shift of the scattering spectrum was observed for IAPPa−Cit AuNP interaction (Figure 4B). This red shift could be induced by the attraction between the oppositely charged Cit AuNPs and IAPP fibrils, which reduced the interparticle distance compared with the nanoparticle control (blue trace), but was still sterically restricted by the large width of IAPPa (ca. 7−12 nm).[3] A larger red shift of 77 nm was obtained for IAPPo−Cit AuNP complexes, due to the further reduced AuNP separations resulting from the smaller dimensions of IAPPo than IAPPa. The strongest plasmonic coupling and largest red shift (119 nm) occurred for IAPPm−Cit AuNPs complexes, a logical outcome given the smallest separations between the Cit AuNPs associated with IAPPm. These results corroborated the experimental observations (Figures 2 and 3; Table 1) that IAPP species at different aggregation stages can significantly impact the plasmonic coupling between IAPP-associated AuNPs (Figure 4C). In light of the significant and unidirectional SPR spectral shifts induced by IAPP in aggregation, especially for Cit AuNPs, HSI may serve as a facile alternative to conventional kinetics assays and electron microscopy for reporting the aggregation states of a range of amyloid proteins.

Circular dichroism (CD) spectroscopy was performed to further probe the secondary structures of the monomeric, oligomeric, and fibrillar IAPP species. IAPPm possessed ∼18%

DOI: 10.1021/acsami.8b19506
ACS Appl. Mater. Interfaces 2019, 11, 10462−10471

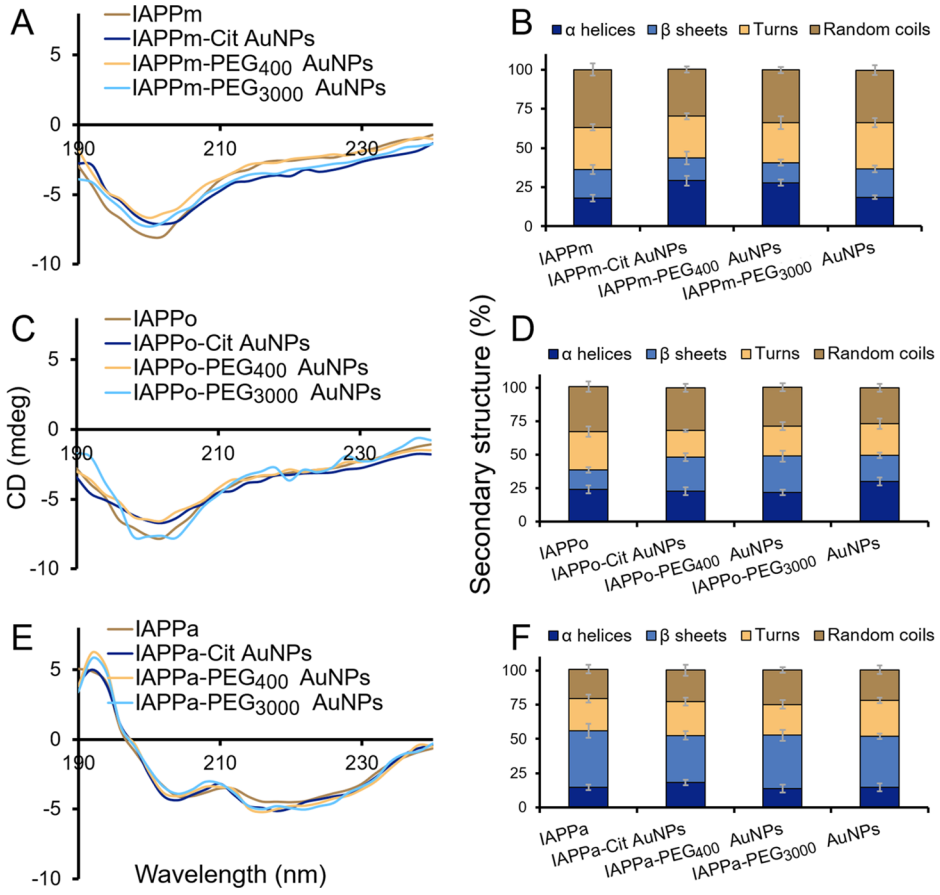

Figure 5. (A, C, E) CD spectra and (B, D, F) percentage secondary structures of IAPPm, IAPPo, and IAPPa in the presence and absence of Cit AuNPs, PEG_{400} AuNPs, and PEG_{3000} AuNPs. IAPP (100 μM) was incubated with 50 μM of AuNPs for 10 min before reading.

of both α helices and β sheets (Figure 5A,B). After binding with Cit AuNPs and PEG_{400} AuNPs, the α-helix content increased to 29 and 27%, whereas the β-sheet content reduced to 14 and 12%, respectively (Figure 5A,B), which is comparable to the structural composition of IAPPo. IAPPo, upon binding with Cit AuNPs and PEG_{400} AuNPs, assumed 25 and 27% of β sheets, respectively (Figure 5C,D). In contrast, PEG_{3000} AuNPs did not induce any conformational changes in IAPP after binding with IAPPm, IAPPo, and IAPPa. In the case of IAPPa, none of the three types of AuNPs were able to trigger any conformational change in tightly packed β-sheets of IAPPa (Figure 5E,F). A ThT kinetic assay further showed that Cit AuNPs and PEG_{400} AuNPs induced early oligomerization of IAPP monomers and faster fibrillation of IAPP oligomers into β-sheet-rich fibrils (Figure S4). In addition, the faster fibrillization effect was found to be dependent upon the concentration (10−1.25 μM) of all three types of AuNPs (Figure S5). Apart from the concentration, the size of nanoparticles has also been found to influence the aggregation kinetics of proteins in the literature.[32,33] It should be noted that although ThT measured the ensemble average of IAPP aggregation kinetics in the presence of AuNPs, HSI allowed for AuNP−protein interaction and AuNP corona formation to be obtained on the single-particle level and with significant statistics. Therefore, these two techniques are complementary in describing the effects of (metal) nanoparticles on protein aggregation and inhibition.

Immune Responses of T Cells to Three IAPP Aggregation States without AuNPs. Current in vitro studies of IAPP toxicity typically focus on cell viability, whereas the immune responses to amyloid proteins in various aggregation states, especially in the presence of nanoparticle inhibitors, have rarely been examined. Recent evidence suggests that IAPP aggregates can trigger the upregulation of proinflammatory cytokines to impair β-cell insulin secretion.[34,35] Unveiling the pathological mechanisms of IAPP-induced immune responses can thus provide an alternative strategy based on anti-inflammatory therapies for protecting IAPP-induced β-cell dysfunction.[36] Previous works investigating IAPP-associated immune responses mainly relied on the "gold standard" enzyme-linked immunosorbent assay (ELISA), which requires a typical assay time of 4−8 h. The complicated sample preparation and long assay time of ELISA pose significant challenges for monitoring the dynamic secretion of immune cells upon IAPP exposure, especially considering the rapid monomer to fibril transformation of the peptide. Recently, we reported a microfluidic-based LSPR platform, which allowed rapid and sensitive detection of multiple cytokines in biological samples simultaneously.[37] In this study, the label-free and ease of integration characteristics of the LSPR platform provided a near-real-time detection scheme for on-chip determination of cellular immune responses to the three IAPP forms as well as their associated AuNP complexes.

Jurkat human T cells were selected as a model system to investigate the IAPP and AuNP−IAPP "corona" induced immune responses.[38] The immune cell secretion after stimulation was assessed by quantifying two critical proinflammatory cytokines: tumor necrosis factor-α (TNF-α) and

DOI: 10.1021/acsami.8b19506
ACS Appl. Mater. Interfaces 2019, 11, 10462−10471

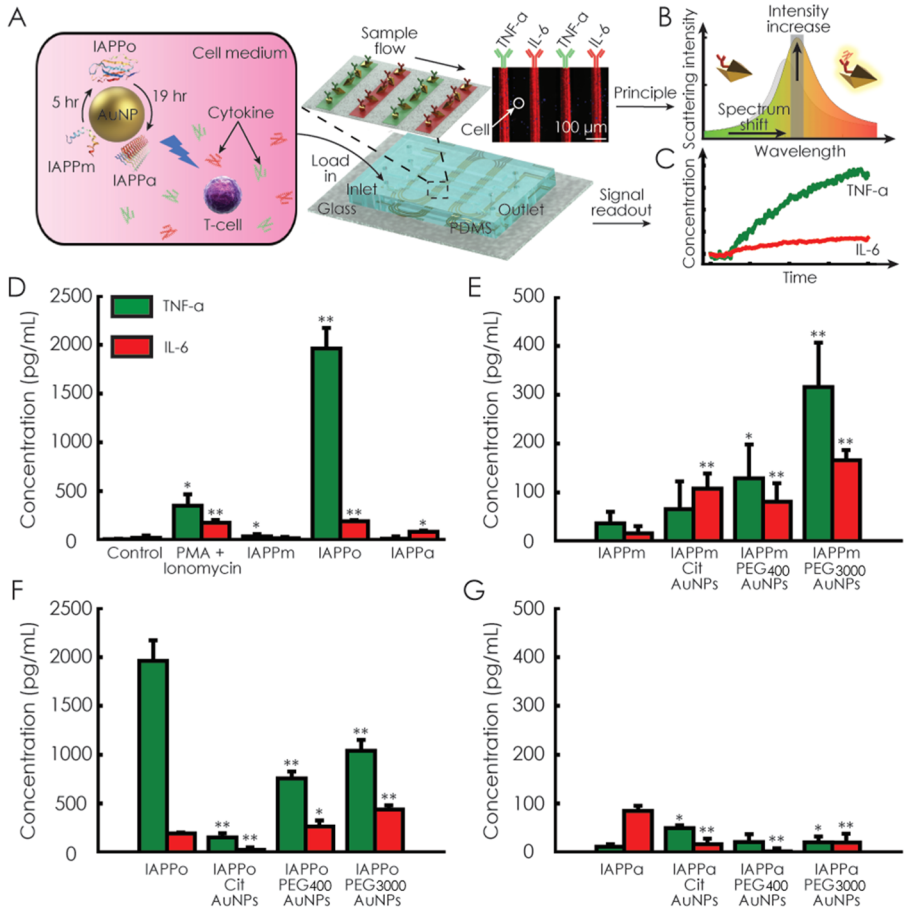

Figure 6. (A) LSPR immunoassay for IAPP- and AuNP−IAPP-induced T-cell immune response detection. Jurkat T cells were stimulated by as-prepared pure IAPP or AuNP−IAPP coronas, and the cellular immune response was determined by simultaneously measuring the TNF-α and IL-6 concentrations in the collected cell culture medium using the LSPR microfluidic chip. (B) Specific binding events occurring on the AuNBP surface yielded a localized refractive index change and a larger scattering cross section, resulting in a red-shifted peak and an increased scattering intensity. By employing a band-pass filter (645−695 nm) and an EMCCD, the secretory cytokine levels were quantified by measuring the scattering light intensity changes at the designed resonance wavelengths. (C) Representative real-time detection curves of cytokine concentrations for T cells stimulated with IAPPo. (D) Cytokine secretion profiles of T cells for the control, PMA + ionomycine (positive control), IAPPm, IAPPo, and IAPPa stimulation. Cytokine secretion profiles for T cells activated by (E) IAPPm, (F) IAPPo, and (G) IAPPa in the presence of the three types of AuNPs. Data represent the mean ± standard error of the mean with $n \geq 3$. P values were calculated using Student's t-test. *$P < 0.05$; **$P < 0.01$.

interleukin 6 (IL-6). The three states of IAPP and the AuNP−IAPP complexes were prepared as illustrated in Figure 6A. After incubation with the T cells, the cell culture medium was collected and loaded into the prepared LSPR chip (Figure S6). The binding of secretory cytokines on antibody-functionalized gold nanobipyramids (AuNBPs) led to plasmon resonance spectrum red shifts and increased scattering intensities (Figure 6B). The optical signals were collected by an electron-multiplying charge-coupled device (EMCCD) in real-time and were converted into cytokine concentrations according to the established standard curves (Figures 6C and S7). To validate the LSPR immunoassay, phorbol 12-myristate 13-acetate (PMA)/ionomycin-stimulated T cells were used as positive controls, showing significantly higher cytokine secretion levels than nonactivated T cells (control) (Figure 6D).[39] Among the three IAPP species, IAPPo induced pronounced inflammatory responses from T cells, as indicated by the high level of TNF-α secretion (~2000 pg/mL), whereas IAPPm and IAPPa elicited no significant cytokine secretions. This is consistent with the finding that IAPP in the low order of oligomerization form can provide a Toll-like receptor 2-dependent stimulus for NF-κB activation,[36] a known pathway for the expression of TNF-α.[40]

Interestingly, the T cells displayed a completely different cytokine release after incubating with the three types of AuNP−IAPP protein coronas. As indicated in Figure 6E, AuNP−IAPPm coronas induced a relatively higher amount of inflammatory cytokine secretions from T cells than the control IAPPm. This could be attributed to the promoted close packing of IAPPm on the AuNPs and thus accelerated oligomerization from IAPPm to IAPPo, as evidenced by our CD and ThT assays where similar structural compositions of α helices and β sheets were observed for AuNP−IAPPm corona and pure IAPPo. In contrast, a noticeable reduction of secretory cytokines was observed from T cells treated with AuNP−IAPPo (Figure 6F). Such inhibited immune responses may be consequential to the increased peptide dimensions and altered secondary structure of the peptide after AuNP adsorption, thereby prohibiting the interaction between IAPPo and the T-cell surface receptor.[41] The T cells showed minimal immune responses to IAPPa and AuNP−IAPPa coronas, which strongly agrees with our observations that IAPPa was less toxic than oligomers and remained structurally stable after incubating with AuNPs (Figure 6G).

DOI: 10.1021/acsami.8b19506
ACS Appl. Mater. Interfaces 2019, 11, 10462−10471

It is known that the surface morphology and chemistry of AuNPs can elicit physicochemical and pathological changes in protein conformation upon nanoparticle−protein interactions.[42,43] Our results suggest that the smaller sized Cit AuNPs facilitated their interactions with IAPPm and IAPPo with considerable secondary structure changes induced resulting from their larger surface curvatures and higher surface energies as compared to the PEGylated AuNPs. This could lead to the unfolding of IAPP and alter the subsequent T-cell immune responses. The attachment of long PEG chains on the AuNPs imposed a steric hindrance and entailed strong antipeptide fouling and less protein misfolding. As such, the differential immune responses from T cells triggered by IAPP and AuNP−IAPP species may be understood as consequential to the structural and toxicity profiles of the three states of IAPP as well as the differential physicochemical properties of the AuNPs derived from their surface ligands.

CONCLUSIONS

In summary, we have demonstrated HSI and LSPR platforms as two new strategies for differentiating the aggregation states of human IAPPs and their elicited immune responses in T cells. In the HSI scheme, the monomeric, oligomeric/protofibrillar, and fibrillar IAPP states spatially separated ligand-coated AuNPs, which translated to easily discernable, unidirectional SPR spectral shifts upon light excitation. In the LSPR scheme, the SPR shifts of gold nanobipyramids served as reporters of cytokine secretion by immune cells exposed to IAPP aggregates. IAPPo, being the most toxic form of the three aggregation states, elicited the highest level of TNF-α cytokine secretion, whereas Cit AuNPs were the most effective in suppressing immune responses to IAPPo than PEG_{400} or PEG_{3000} AuNPs. This finding suggests that nanoparticles stabilized with ligands of shorter chain lengths and moderate antifouling capacities (e.g., Cit over PEG_{400} and PEG_{3000}) are more effective reporters of protein aggregation and inhibitors against amyloid protein toxicity. These findings have implications for both fundamental research on protein misfolding and therapeutic development against amyloid diseases with nanotechnologies.

MATERIALS AND METHODS

Syntheses of Ligand-Stabilized AuNPs. Citrate AuNPs (Cit AuNPs) were synthesized by the direct reduction method.[44] Briefly, 10 mL of 1 mM aqueous solution of $HAuCl_4$ was refluxed at 120 °C and 1 mL of 40 mM trisodium citrate was added into the Au solution. The color of the suspension changed to wine red, indicating the formation of 15−20 nm AuNPs. The PEG-stabilized AuNPs were synthesized by ligand replacement.[45] Specifically, 1 mL of Cit AuNPs was mixed with 10 μL of 10% PEG solution of molecular weight 400 or 3000 Da. The suspension was stirred overnight. All AuNPs were purified via centrifugal filtration of 100 kDa MWCO. The concentration of AuNPs was calculated by a reported method.[44,46] The absorbance of the AuNP suspensions was measured with a UV−vis spectrophotometer (PerkinElmer, Enspire).

Preparations of Three IAPP Aggregation States. Human islet amyloid polypeptide, IAPP (KCNTATCATQRLANFLVHSSNNF-GAILSSTNVGSNTY; disulfide bridge: 2−7; AnaSpec, Inc.) was treated with hexafluoro-2-propanol (HFIP) before use. The HFIP-treated IAPP assumed the monomeric form. Oligomeric IAPP was prepared by incubating the HFIP-treated IAPP at 4 °C for 5 h, whereas full-length mature fibrils of IAPP were prepared by incubating the peptide for more than 24 h at room temperature. All three fibrillation states were confirmed by transmission electron microscopy (TEM).

Transmission Electron Microscopy. TEM images were recorded on a Tecnai F20 transmission electron microscope (FEI) at 200 kV with an UltraScan 1000 (2k × 2k) CCD camera (Gatan). A formvar-coated copper mesh grid was glow-discharged, and a drop of sample was blotted on the grid for 60 s. Negative staining with 1% uranyl acetate was applied to improve image contrast.

Toxicities of Ligand-Stabilized AuNPs and IAPP Aggregates. Pancreatic βTC6 (ATCC) β cells were grown in complete Dulbecco's modified Eagle's medium (DMEM) with 15% fetal bovine serum (FBS). To perform the viability experiment, a 96-well plate (Costar black/clear bottom) was coated with 70 μL poly-L-lysine (Sigma, 0.01%) for 30 min at 37 °C. The wells were washed three times with phosphate buffered saline, and ∼60 000 cells in 200 μL DMEM with 15% FBS were added to each well. The cells were incubated for 2 days at 37 °C and 5% CO_2 to reach ∼80% confluency. The cell culture medium was then refreshed, and 1 μM propidium iodide (PI) dye in complete DMEM was added to the wells and incubated for 30 min. For the treatment, 20 μM IAPP (0 h as monomers and 1 h aged as oligomers), 20 μM of Cit AuNPs, PEG_{400} AuNPs, and PEG_{3000} AuNPs, and IAPP preincubated with the AuNPs were added into the wells. After 14 h of treatment, samples were measured by Operetta (PerkinElmer, 20× PlanApo microscope objective, numerical aperture NA = 0.7) in a live cell chamber (37 °C, 5% CO_2). The percentage of dead cells (PI-positive) relative to total cell count was determined by a built-in bright-field mapping function of Harmony High-Content Imaging and Analysis software (PerkinElmer). The measurement was conducted at five reads per well, and all were performed in triplicate. Untreated cells were recorded as controls.

Hyperspectral Imaging (HSI). HSI imaging was performed on a dark-field hyperspectral microscope (CytoViva) fixed with a PixelFly CCD camera (Cooke/PCO, USA/Germany). Images were recorded with 1 s exposure time and analyzed by ENVI 4.8 software. All images were normalized for blank background spectra. SPR spectra for AuNPs were recorded for 10−15 AuNPs across five images and averaged together. To study the interactions of AuNPs with different IAPP species, AuNPs (5 μM) were incubated for 5 min with the IAPP species (25 μM) and a drop of sample was sandwiched between a glass slide and a coverslip and sealed with a slide sealant.

Thioflavin T (ThT) Kinetic Assay. A ThT assay was performed by incubating 100 μL aqueous solution of IAPP (25 μM), ThT (75 μM), and AuNPs (1.25−10 μM) in 96-well microplates at 37 °C. ThT fluorescence readings were recorded with light excitation at 440 nm and emission at 485 nm over a period of 6 h after specified intervals (PerkinElmer, Enspire).

Circular Dichroism (CD) Spectroscopy. CD spectroscopy analysis was performed by mixing the three aggregation states of IAPP, as prepared for TEM, with the three different types of AuNPs. The final concentrations of the IAPP and the AuNPs in the samples were adjusted to 100 and 50 μM, respectively. The incubation time was 10 min before the CD reading. A total of 200 μL of the samples was pipetted into a CD cuvette, and CD spectra were recorded from 190 to 240 nm with 1 nm step size at room temperature. The data was analyzed by Dichroweb (Contin/Reference set 4) for estimation of the percentage secondary content.[47]

COMSOL Calculations. The scattering spectra of Cit AuNP and the three types of IAPP−Cit AuNP complexes were simulated by the finite element method using commercial multiphysics simulation software (COMSOL). Briefly, four simulation models of single Cit AuNPs, IAPPm−Cit AuNPs, IAPPo−Cit AuNPs, and IAPPa−Cit AuNPs were constructed. The far-field domain was set as a semispherical shell with a radius of half the wavelength of the incident light. A perfectly matched layer, serving as the boundary condition of light and with a radius of half the wavelength of the incident light, was then defined on top of the far-field domain. A polarized incident light was set in parallel with the Cit AuNP packing direction. The scattering intensity was evaluated by the scattering cross section C_{SCS} of AuNPs, which is the integration of the scattering wave intensity over the surface of far-domain Ω

DOI: 10.1021/acsami.8b19506
ACS Appl. Mater. Interfaces 2019, 11, 10462−10471

$$C_{SCS} = \int \frac{I_{AuNP}}{I_{background}} d\Omega \quad (1)$$

where I_{AuNP} is the scattering intensity from the AuNPs and $I_{background}$ the background signal without the presence of AuNPs. To simplify computation, Cit AuNPs were treated as single nanospheres with a radius of 11.3 nm. IAPP oligomers/protofibrils and amyloids were simplified as cylinders with radii of 2 and 5 nm, respectively. The frequency-dependent dielectric constant of gold, $\in_1$, was derived from the Lorentz−Drude model

$$\in_1 = 1 - \frac{\omega_p^2}{\omega^2 + \gamma^2} \quad (2)$$

where ω_p is the bulk metal plasmon frequency and γ is the bulk metal damping frequency.[32] The relative permittivities of water and IAPP were fixed as 1.77 and 2.25, respectively.[33] Due to the relatively small dimensions of IAPP monomers, the IAPPm−Cit AuNP model was constructed as pure Cit AuNP aggregates, consisting of 12 Cit AuNPs, whereas Cit AuNPs were assumed to be adsorbed on the fibrils in IAPPa−Cit AuNP and IAPPo−Cit AuNP models. The distances among neighboring AuNPs of the IAPPa−Cit AuNP, IAPPo−Cit AuNP, and IAPPm−Cit AuNP models were defined as 5, 1.2, and 0.7 nm, respectively.

Localized Surface Plasmon Resonance (LSPR) Immunoassay Chip Fabrication. Glass slides were first cleaned by Piranha solution (H_2SO_4/H_2O_2 = 3:1 v/v) for 10 min, followed by deionized water rinsing. The Piranha-cleaned slides were kept in an ultrasonic bath for 15 min and then thoroughly rinsed with deionized water. To create a negatively charged surface, the slides were treated by oxygen plasma for 2 min at 20 W (PE-50, Plasma Etch Inc.) (Figure S6A). The poly(dimethylsiloxane) (PDMS) patterning layer was quickly attached on the plasma-treated glass so that the positively charged cetyltrimethylammonium bromide (CTAB)-capped AuNBPs were immobilized onto the glass surface due to electrostatic interactions after overnight incubation. The AuNBPs used in the LSPR chip were prepared by a two-step method reported previously.[48] Unbound AuNBPs were washed by deionized water, and then 1 mM 11-mercaptoundecanoic acid (Sigma-Aldrich) was loaded to replace the CTAB layer on the surface of AuNBPs and served as linkers for further functionalization. After 12 h incubation, 0.1 M NHS (*N*-hydroxysuccinimide, Thermo Scientific) and 0.4 M EDC (1-ethyl-3-[3-(dimethylamino)propyl]carbodiimide hydrochloride, Thermo Scientific) were mixed (1:1 v/v) in 0.1 M MES (1-ethyl-3-[3-(dimethylamino)propyl]carbodiimide hydrochloride, Thermo Scientific) buffer. The EDC/NHS solution was loaded into microfluidics channels at 2 μL/min for 8 min to activate the ligand and then incubated for 40 min. Probe antibody solutions (antihuman IL-6 and antihuman TNF-α, ebioscience) in 1× phosphate buffered saline (PBS) were injected into different channels and incubated for 1 h. Between each step, the AuNBP microarray was washed by 1× PBS at 2 μL/min for 8 min to remove any excessive molecules. After the antibody functionalization process, the patterning PDMS layer was peeled off and another piece of the PDMS layer with sample loading channels was immediately attached perpendicularly to the barcode patterns.

LSPR Detection of T-Cell Immune Responses to IAPP. Jurkat human T cells (CRL-2901TM, ATCC) were cultured in RPMI-1640 with 200 mcg/mL G428 and 10% fetal bovine serum. The cells were incubated at 37 °C with 5% CO_2 in a Cell Culture Incubator (Thermo Scientific). The culture medium was replaced two to three times per week to maintain the suitable concentration of 1×10^5 to 1×10^6 cells/mL. The cells were collected through centrifugation at 125*g* for 5 min with subsequent resuspension in fresh culture medium.

For the IAPP control experiments, freshly prepared IAPP was diluted in 1× PBS to 50 μM. IAPPm solution (1 μL) was immediately added to 1 mL culture medium with T cells at 1×10^6 cells/mL and incubated for 2 h. The remaining IAPPm solutions were incubated at 4 °C for 5 h (IAPPo) and 24 h (IAPPa). After that, 10 μL of a supernatant was collected from the T-cell culture medium for the LSPR immunoassay. The same procedure was repeated for IAPPo- and IAPPa-stimulated T cells. For the AuNP−IAPP corona experiments, nine types of IAPP−AuNP complexes were prepared by mixing 100 μM IAPP solution with 1 mM AuNP solution at a 1:1 molar ratio and incubated for 5 min. The same steps were conducted to activate the T cells and perform the LSPR immunoassay.

■ ASSOCIATED CONTENT

Supporting Information

The Supporting Information is available free of charge on the ACS Publications website at DOI: 10.1021/acsami.8b19506.

DLS, ζ-potential, HSI, UV−vis, cell viability, ThT kinetic assays, and LSPR immunoassay; hydrodynamic sizes, polydispersity indexes (PDI), and ζ-potentials of IAPPm, IAPPo, and IAPPa with and without incubation with the three types of AuNPs. Incubation time: 5 min (Table S1); in vitro toxicities of IAPPm (0 h) and IAPPo (1 h) (20 μM) in βTC6 cells in the presence and absence of 20 μM Cit AuNPs, PEG_{400}, and PEG_{3000} AuNPs. The assay was carried out in triplicate. The error bars show the standard deviations of the averaged data sets (Figure S1); dependence of HSI spectral shifts of Cit AuNPs on the concentration of IAPPm. Cit AuNPs: 5 μM. Incubation: 5 min (Figure S2); dependence of UV−vis absorbance of Cit AuNPs on the concentration of IAPPm. Cit AuNPs: 5 μM. Incubation: 5 min (Figure S3); ThT kinetic assay on the effects of Cit, PEG_{400}, and PEG_{3000} AuNPs on IAPP fibrillation. The IAPP concentration was fixed at 25 μM, whereas the concentrations of all AuNPs were set at 10 μM. Cit, PEG_{400}, and PEG_{3000} AuNPs did not produce notable ThT background fluorescence. The AuNPs were able to speed up the process of IAPP fibrillation in the order of Cit AuNPs > PEG_{400} AuNPs > PEG_{3000} AuNPs (Figure S4); ThT kinetic assay showing the concentration dependence of three different types of AuNPs on IAPP fibrillation. (A) Cit AuNPs asserted the strongest influence on IAPP fibrillation when their concentration was altered from 10 to 1.25 μM, followed by (B) PEG_{400} and (C) PEG_{3000} AuNPs (Figure S5); (A) illustration of the preparation processes for LSPR immunoassay. The glass slide was first plasma-treated to generate a negatively charged surface and then a PDMS patterning layer was placed on the glass. Due to electrostatic interaction, the CTAB-capped AuNBPs loaded through the PDMS channels were immobilized on a glass surface and formed a barcode pattern. TNF-α and IL-6 antibodies were then injected and conjugated to the AuNBPs by the standard EDC/NHS chemistry. (B) Schematics of the LSPR sensing setup consisting of a dark-field microscope, an EMCCD, and an LSPR immunoassay chip. Scattering light was collected through a 10× objective lens and filtered by a band-pass filter (670 ± 25 nm, Chroma). The optical signal was analyzed by a customized Matlab code. (C) LSPR immunoassay chip mounted under a dark-field microscope. Before each measurement, the chip was completely stabilized by T-cell medium to ensure that the detected signals resulted from the binding of the secretory cytokines on the antibody-coated AuNBPs (Figure S6); (A) intensity mapping of the LSPR immunoassay barcodes for TNF-α and IL-6 at different concentrations. (B) Calibration curves of TNF-α and IL-

DOI: 10.1021/acsami.8b19506
ACS Appl. Mater. Interfaces 2019, 11, 10462−10471

6. The limit of detection (LOD) was determined by the three standard deviations of a blank sample over the slope of the corresponding calibration curve. The LOD was calculated to be 34.1 pg/mL for IL-6 and 45.6 pg/mL for TNF-α (Figure S7) (PDF)

AUTHOR INFORMATION

Corresponding Authors

*E-mail: thomas.p.davis@monash.edu (T.P.D.).
*E-mail: pu-chun.ke@monash.edu (P.C.K.).
*E-mail: pengyuc@auburn.edu (P.C.).

ORCID

Ibrahim Javed: 0000-0003-1101-5614
Thomas P. Davis: 0000-0003-2581-4986
Pu Chun Ke: 0000-0003-2134-0859
Pengyu Chen: 0000-0003-3380-872X

Author Contributions

§I.J. and J.H. contributed equally to this work.

Author Contributions

P.C.K., I.J., P.C., and T.P.D. conceived the project. I.J. performed nanomaterials syntheses, HSI, TEM, and UV−vis assays. I.J. and A.K. conducted CD spectroscopy. A.F. performed the cell culture and viability assay. J.H., W.Y., and P.C. performed COMSOL simulations and LSPR immunoassay. A.K. conducted data analysis and designed the illustrations. P.C.K., I.J., J.H., and P.C. wrote the article. All authors discussed the data and agreed on the manuscript.

Notes

The authors declare no competing financial interest.

ACKNOWLEDGMENTS

The work was partially supported by the ARC Project No. CE140100036 (T.P.D.) and the National Science Foundation Grant No. CBET-1701363 (P.C.). I.J. acknowledges the support of the Monash International Postgraduate Research Scholarship (MIPRS), the Australian Government Research Training Program Scholarship, and the Shanghai Science and Technology Commission "The Belt and Road Initiative" program, Grant No. 17230743000.

REFERENCES

(1) Zraika, S.; Hull, R. L.; Verchere, C. B.; Clark, A.; Potter, K. J.; Fraser, P. E.; Raleigh, D. P.; Kahn, S. E. Toxic Oligomers and Islet Beta Cell Death: Guilty by Association or Convicted by Circumstantial Evidence? *Diabetologia* **2010**, *53*, 1046−1056.

(2) Schmitz, O.; Brock, B.; Rungby, J. Amylin Agonists: A Novel Approach in the Treatment of Diabetes. *Diabetes* **2004**, *53*, S233−S238.

(3) Ke, P. C.; Sani, M.-A.; Ding, F.; Kakinen, A.; Javed, I.; Separovic, F.; Davis, T. P.; Mezzenga, R. Implications of Peptide Assemblies in Amyloid Diseases. *Chem. Soc. Rev.* **2017**, *46*, 6492−6531.

(4) Haataja, L.; Gurlo, T.; Huang, C. J.; Butler, P. C. Islet Amyloid in Type 2 Diabetes, and the Toxic Oligomer Hypothesis. *Endocr. Rev.* **2008**, *29*, 303−316.

(5) Javed, I.; Yu, T.; Peng, G.; Sánchez-Ferrer, A.; Faridi, A.; Kakinen, A.; Zhao, M.; Mezzenga, R.; Davis, T. P.; Lin, S.; Ke, P. C. In Vivo Mitigation of Amyloidogenesis through Functional−Pathogenic Double-Protein Coronae. *Nano Lett.* **2018**, *18*, 5797−5804.

(6) DeToma, A. S.; Salamekh, S.; Ramamoorthy, A.; Lim, M. H. Misfolded Proteins in Alzheimer's Disease and Type Ii Diabetes. *Chem. Soc. Rev.* **2012**, *41*, 608−621.

(7) Eisenberg, D.; Jucker, M. The Amyloid State of Proteins in Human Diseases. *Cell* **2012**, *148*, 1188−1203.

(8) Knowles, T. P.; Vendruscolo, M.; Dobson, C. M. The Amyloid State and Its Association with Protein Misfolding Diseases. *Nat. Rev. Mol. Cell Biol.* **2014**, *15*, 384−396.

(9) Kakinen, A.; Sun, Y.; Javed, I.; Faridix, A.; Pilkington, E. H.; Faridi, P.; Purcell, A. W.; Zhou, R.; Ding, F.; Lin, S.; Ke, P. C.; Davis, T. P. Physical and Toxicological Profiles of Human Iapp Amyloids and Plaques. *Sci. Bull.* **2019**, *64*, 26−35.

(10) Li, L.; Guest, W.; Huang, A.; Plotkin, S. S.; Cashman, N. R. Immunological Mimicry of Prpc−Prpsc Interactions: Antibody-Induced Prp Misfolding. *Protein Eng., Des. Sel.* **2009**, *22*, 523−529.

(11) Honig, L. S.; Vellas, B.; Woodward, M.; Boada, M.; Bullock, R.; Borrie, M.; Hager, K.; Andreasen, N.; Scarpini, E.; Liu-Seifert, H.; et al. Trial of Solanezumab for Mild Dementia Due to Alzheimer's Disease. *New Engl. J. Med.* **2018**, *378*, 321−330.

(12) Abbott, A.; Dolgin, E. Failed Alzheimer's Trial Does Not Kill Leading Theory of Disease. *Nature* **2016**, *540*, 15−16.

(13) Sevigny, J.; Chiao, P.; Bussière, T.; Weinreb, P. H.; Williams, L.; Maier, M.; Dunstan, R.; Salloway, S.; Chen, T.; Ling, Y.; et al. The Antibody Aducanumab Reduces Aβ Plaques in Alzheimer's Disease. *Nature* **2016**, *537*, 50−56.

(14) Kayed, R.; Head, E.; Sarsoza, F.; Saing, T.; Cotman, C. W.; Necula, M.; Margol, L.; Wu, J.; Breydo, L.; Thompson, J. L.; Rasool, S. Fibril Specific, Conformation Dependent Antibodies Recognize a Generic Epitope Common to Amyloid Fibrils and Fibrillar Oligomers That Is Absent in Prefibrillar Oligomers. *Mol. Neurodegener.* **2007**, *2*, 18.

(15) Hefti, F.; Goure, W. F.; Jerecic, J.; Iverson, K. S.; Walicke, P. A.; Krafft, G. A. The Case for Soluble Aβ Oligomers as a Drug Target in Alzheimer's Disease. *Trends Pharmacol. Sci.* **2013**, *34*, 261−266.

(16) Kayed, R.; Head, E.; Thompson, J. L.; McIntire, T. M.; Milton, S. C.; Cotman, C. W.; Glabe, C. G. Common Structure of Soluble Amyloid Oligomers Implies Common Mechanism of Pathogenesis. *Science* **2003**, *300*, 486−489.

(17) Javed, I.; Sun, Y.; Adamcik, J.; Wang, B.; Kakinen, A.; Pilkington, E. H.; Ding, F.; Mezzenga, R.; Davis, T. P.; Ke, P. C. Cofibrillization of Pathogenic and Functional Amyloid Proteins with Gold Nanoparticles against Amyloidogenesis. *Biomacromolecules* **2017**, *18*, 4316−4322.

(18) Faridi, A.; Sun, Y.; Okazaki, Y.; Peng, G.; Gao, J.; Kakinen, A.; Faridi, P.; Zhao, M.; Javed, I.; Purcell, A. W.; Davis, T. P. Mitigating Human Iapp Amyloidogenesis in Vivo with Chiral Silica Nanoribbons. *Small* **2018**, *14*, 1802825.

(19) Gowen, A.; O'Donnell, C.; Cullen, P.; Downey, G.; Frias, J. Hyperspectral Imaging−an Emerging Process Analytical Tool for Food Quality and Safety Control. *Trends Food Sci. Technol.* **2007**, *18*, 590−598.

(20) Wen, Y.; Geitner, N. K.; Chen, R.; Ding, F.; Chen, P.; Andorfer, R. E.; Govindan, P. N.; Ke, P. C. Binding of Cytoskeletal Proteins with Silver Nanoparticles. *RSC Adv.* **2013**, *3*, 22002−22007.

(21) Lim, D.-H.; Jang, J.; Kim, S.; Kang, T.; Lee, K.; Choi, I.-H. The Effects of Sub-Lethal Concentrations of Silver Nanoparticles on Inflammatory and Stress Genes in Human Macrophages Using Cdna Microarray Analysis. *Biomaterials* **2012**, *33*, 4690−4699.

(22) Smith, B. R.; Ghosn, E. E. B.; Rallapalli, H.; Prescher, J. A.; Larson, T.; Herzenberg, L. A.; Gambhir, S. S. Selective Uptake of Single-Walled Carbon Nanotubes by Circulating Monocytes for Enhanced Tumour Delivery. *Nat. Nanotechnol.* **2014**, *9*, 481−487.

(23) Mortimer, M.; Gogos, A.; Bartolomé, N.; Kahru, A.; Bucheli, T. D.; Slaveykova, V. I. Potential of Hyperspectral Imaging Microscopy for Semi-Quantitative Analysis of Nanoparticle Uptake by Protozoa. *Environ. Sci. Technol.* **2014**, *48*, 8760−8767.

(24) Badireddy, A. R.; Wiesner, M. R.; Liu, J. Detection, Characterization, and Abundance of Engineered Nanoparticles in Complex Waters by Hyperspectral Imagery with Enhanced Darkfield Microscopy. *Environ. Sci. Technol.* **2012**, *46*, 10081−10088.

DOI: 10.1021/acsami.8b19506
ACS Appl. Mater. Interfaces 2019, 11, 10462−10471

(25) Ding, F.; Radic, S.; Chen, R.; Chen, P.; Geitner, N. K.; Brown, J. M.; Ke, P. C. Direct Observation of a Single Nanoparticle−Ubiquitin Corona Formation. *Nanoscale* **2013**, *5*, 9162−9169.
(26) Schöttler, S.; Becker, G.; Winzen, S.; Steinbach, T.; Mohr, K.; Landfester, K.; Mailänder, V.; Wurm, F. R. Protein Adsorption Is Required for Stealth Effect of Poly (Ethylene Glycol)-and Poly (Phosphoester)-Coated Nanocarriers. *Nat. Nanotechnol.* **2016**, *11*, 372−377.
(27) Chen, G.; Roy, I.; Yang, C.; Prasad, P. N. Nanochemistry and Nanomedicine for Nanoparticle-Based Diagnostics and Therapy. *Chem. Rev.* **2016**, *116*, 2826−2885.
(28) Blanco, E.; Shen, H.; Ferrari, M. Principles of Nanoparticle Design for Overcoming Biological Barriers to Drug Delivery. *Nat. Biotechnol.* **2015**, *33*, 941−951.
(29) Mahmoud, M. A.; Chamanzar, M.; Adibi, A.; El-Sayed, M. A. Effect of the Dielectric Constant of the Surrounding Medium and the Substrate on the Surface Plasmon Resonance Spectrum and Sensitivity Factors of Highly Symmetric Systems: Silver Nanocubes. *J. Am. Chem. Soc.* **2012**, *134*, 6434−6442.
(30) Mahmoud, M.; Snyder, B.; El-Sayed, M. Surface Plasmon Fields and Coupling in the Hollow Gold Nanoparticles and Surface-Enhanced Raman Spectroscopy. Theory and Experiment. *J. Phys. Chem. C* **2010**, *114*, 7436−7443.
(31) Mahmoud, M.; El-Sayed, M. Aggregation of Gold Nanoframes Reduces, Rather Than Enhances, Sers Efficiency Due to the Trade-Off of the Inter-and Intraparticle Plasmonic Fields. *Nano Lett.* **2009**, *9*, 3025−3031.
(32) Álvarez, Y. D.; Fauerbach, J. A.; Pellegrotti, J. V.; Jovin, T. M.; Jares-Erijman, E. A.; Stefani, F. D. Influence of Gold Nanoparticles on the Kinetics of A-Synuclein Aggregation. *Nano Lett.* **2013**, *13*, 6156−6163.
(33) Álvarez, Y. D.; Pellegrotti, J. V.; Stefani, F. D. Gold Nanoparticles as Nucleation Centers for Amyloid Fibrillation. In *Use of Nanoparticles in Neuroscience*; Springer, 2018; pp 269−291.
(34) Corbett, J. A.; Wang, J.; Sweetland, M.; Lancaster, J. R.; McDaniel, M. Interleukin 1 Beta Induces the Formation of Nitric Oxide by Beta-Cells Purified from Rodent Islets of Langerhans. Evidence for the Beta-Cell as a Source and Site of Action of Nitric Oxide. *J. Clin. Invest.* **1992**, *90*, 2384−2391.
(35) Bendtzen, K.; Mandrup-Poulsen, T.; Nerup, J.; Nielsen, J. H.; Dinarello, C. A.; Svenson, M. Cytotoxicity of Human Pi 7 Interleukin-1 for Pancreatic Islets of Langerhans. *Science* **1986**, *232*, 1545−1547.
(36) Westwell-Roper, C.; Denroche, H. C.; Ehses, J. A.; Verchere, C. B. Differential Activation of Innate Immune Pathways by Distinct Islet Amyloid Polypeptide (Iapp) Aggregates. *J. Biol. Chem.* **2016**, *291*, 8908−8917.
(37) Chen, P.; Chung, M. T.; McHugh, W.; Nidetz, R.; Li, Y.; Fu, J.; Cornell, T. T.; Shanley, T. P.; Kurabayashi, K. Multiplex Serum Cytokine Immunoassay Using Nanoplasmonic Biosensor Microarrays. *ACS Nano* **2015**, *9*, 4173−4181.
(38) Cedervall, T.; Lynch, I.; Lindman, S.; Berggård, T.; Thulin, E.; Nilsson, H.; Dawson, K. A.; Linse, S. Understanding the Nanoparticle−Protein Corona Using Methods to Quantify Exchange Rates and Affinities of Proteins for Nanoparticles. *Proc. Natl. Acad. Sci. U.S.A.* **2007**, *104*, 2050−2055.
(39) Ai, W.; Li, H.; Song, N.; Li, L.; Chen, H. Optimal Method to Stimulate Cytokine Production and Its Use in Immunotoxicity Assessment. *Int. J. Environ. Res.* **2013**, *10*, 3834−3842.
(40) Baud, V.; Karin, M. Signal Transduction by Tumor Necrosis Factor and Its Relatives. *Trends Cell Biol.* **2001**, *11*, 372−377.
(41) Jiang, W.; Kim, B. Y. S.; Rutka, J. T.; Chan, W. C. W. Nanoparticle-Mediated Cellular Response Is Size-Dependent. *Nat. Nanotechnol.* **2008**, *3*, 145−150.
(42) Deng, Z. J.; Liang, M.; Monteiro, M.; Toth, I.; Minchin, R. F. Nanoparticle-Induced Unfolding of Fibrinogen Promotes Mac-1 Receptor Activation and Inflammation. *Nat. Nanotechnol.* **2011**, *6*, 39−44.
(43) Lynch, I.; Salvati, A.; Dawson, K. A. What Does the Cell See? *Nat. Nanotechnol.* **2009**, *4*, 546−547.
(44) Haiss, W.; Thanh, N. T.; Aveyard, J.; Fernig, D. G. Determination of Size and Concentration of Gold Nanoparticles from UV−Vis Spectra. *Anal. Chem.* **2007**, *79*, 4215−4221.
(45) Javed, I.; Hussain, S. Z.; Shahzad, A.; Khan, J. M.; Rehman, M.; Usman, F.; Razi, M. T.; Shah, M. R.; Hussain, I. Lecithin-Gold Hybrid Nanocarriers as Efficient and Ph Selective Vehicles for Oral Delivery of Diacerein—in-Vitro and in-Vivo Study. *Colloids Surf., B* **2016**, *141*, 1−9.
(46) Liu, X.; Atwater, M.; Wang, J.; Huo, Q. Extinction Coefficient of Gold Nanoparticles with Different Sizes and Different Capping Ligands. *Colloids Surf., B* **2007**, *58*, 3−7.
(47) Whitmore, L.; Wallace, B. A. Protein Secondary Structure Analyses from Circular Dichroism Spectroscopy: Methods and Reference Databases. *Biopolymers* **2008**, *89*, 392−400.
(48) Li, Q.; Zhuo, X.; Li, S.; Ruan, Q.; Xu, Q.-H.; Wang, J. Production of Monodisperse Gold Nanobipyramids with Number Percentages Approaching 100% and Evaluation of Their Plasmonic Properties. *Adv. Opt. Mater.* **2015**, *3*, 801−812.

DOI: 10.1021/acsami.8b19506
ACS Appl. Mater. Interfaces 2019, 11, 10462−10471